

MoD-SLAM: Monocular Dense Mapping for Unbounded 3D Scene Reconstruction

Heng Zhou¹, Zhetao Guo⁴, Shuhong Liu², Lechen Zhang¹, Qihao Wang¹,
Yuxiang Ren⁵, and Mingrui Li^{3*}

¹ Columbia University {hz2944,lechen.zhang,qw2414}@mail.dlut.edu.cn

² The University of Tokyo {s-liu}@isi.imi.i.u-tokyo.ac.jp

³ Dalian University of Technology {2905450254}@mail.dlut.edu.cn

⁴ Cloudspace Technology {gzt}@yhsk.com.cn

⁵ Dianjing Ci yuan Culture {yuxiang.ren}@dianjcy.com

Abstract. Neural implicit representations have recently been demonstrated in many fields including Simultaneous Localization And Mapping (SLAM). Current neural SLAM can achieve ideal results in reconstructing bounded scenes, but this relies on the input of RGB-D images. Neural-based SLAM based only on RGB images is unable to reconstruct the scale of the scene accurately, and it also suffers from scale drift due to errors accumulated during tracking. To overcome these limitations, we present MoD-SLAM, a monocular dense mapping method that allows global pose optimization and 3D reconstruction in real-time in unbounded scenes. Optimizing scene reconstruction by monocular depth estimation and using loop closure detection to update camera pose enable detailed and precise reconstruction on large scenes. Compared to previous work, our approach is more robust, scalable and versatile. Our experiments demonstrate that MoD-SLAM has more excellent mapping performance than prior neural SLAM methods, especially in large borderless scenes.

Keywords: 3D scene reconstruction, neural radiance field, SLAM, monocular depth estimation, unbounded scene

1 Introduction

Dense visual Simultaneous Localization and Mapping (SLAM) is core in 3D computer vision, finding utility across various fields including autonomous driving, unmanned aerial vehicle, AR, etc. To make SLAM valuable in real-world applications, we want SLAM to be real-time, fast, accurate, and adaptable to scenes of different scales. Although traditional SLAM methods [4,17,46] can build maps in real-time, they can only generate sparse maps. Some works [31,43,46] can generate dense maps to a certain extent, but both of them are generally too slow to build maps and can not be applied to large unbounded scenes. These constraints limit the application of SLAM.

In recent years, due to the development and advancement of Neural Radiance Field (NeRF) [15,8] and view synthesis [19,26,1] in 3D scene reconstruction,

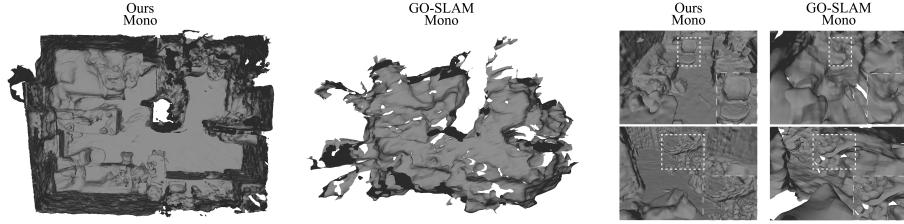


Fig. 1: Reconstruction results on ScanNet. We present MoD-SLAM, a neural-based monocular dense mapping method. Our method shows a more powerful capability than existing work: GO-SLAM [42].

dense SLAM mapping has become feasible. Early NeRF-based SLAM systems such as iMAP [30] and NICE-SLAM [45] have achieved good results in dense mapping and tracking. However, they all have the problems of decreasing accuracy and scale drift in large scenes. Subsequent researches [41,42,37,6,25] apply the signed distance function (SDF) [22] to reconstruct the 3D scene more accurately, but it still can not be implemented in unbounded scenes. Furthermore, numerous works rely on RGB-D input, which fails to adequately reconstruct the scale of the scene, the texture structure, and the details of geometric objects in the monocular mode. These problems limit the application and performance of neural-based SLAM systems in large scenes or scenes with numerous objects and texture details. GO-SLAM [42] tries to input RGB images for 3D scene reconstruction, but the result is unsatisfactory. It lacks the prior depth maps and thus, cannot properly reconstruct the scale of the scene (Fig.1). In addition, numerous previous works lack a loop closure detection, which leads to misalignment and performance degradation in large-scale settings. Therefore, these methods are limited to more controlled and smaller room-scale scenes.

In this work, we propose MoD-SLAM, a monocular implicit neural-based dense mapping method. In contrast to previous works, our SLAM system no longer relies on RGB-D image inputs. It improves its accuracy by incorporating a monocular depth estimation module and a depth distillation module at the backend. These two modules allow the system to generate prior depth maps from the acquired RGB images for supervised 3D scene reconstruction. In addition, we use the Gaussian encoding that approximates the conic truncation corresponding to the pixel as input to MLPs [34] to allow the system to adapt and capture spatial information more precisely. Moreover, we present reparameterization, which enables our SLAM system to achieve ideal reconstruction results in unbounded scenes. We also include loop closure detection in the global update so that the system can combat scale drift. Extensive evaluations on a wide range of indoor RGB sequences demonstrate the scalability and predictive power of our approach. Overall, we make the following contributions:

- A novel NeRF-based dense SLAM system that can handle RGB input conditions and allow high-quality novel view synthesis by using depth estimation

- A ray reparameterization and a Gaussian encoding input that represents the region over which the radiance field should be integrated for neural fields to efficiently represent unbounded scenes.
- We demonstrate state-of-the-art performance on scene reconstruction based on multiple datasets and show competitive results with recent SLAM systems.

2 Related work

Monocular Visual SLAM In the realm of robotic navigation and augmented reality, Simultaneous Localization and Mapping (SLAM) plays a pivotal role. Monocular Visual SLAM, relying solely on a single camera, has attracted significant attention due to its cost-effectiveness and applicability in GPS-denied environments. This technique constructs the 3D map of the surroundings while simultaneously estimating the camera’s position and orientation within that map. By processing sequential frames of video, monocular SLAM algorithms detect and track visual features across images, using them to calculate depth and structure from motion. Some works focused on using more efficient data structures like VoxelHashing [5,27,20] and Octrees [35,39] to improve performance. The most notable method in this domain is ORB-SLAM3 [4], a versatile and accurate system that utilizes ORB features to achieve robust tracking and mapping under a wide range of conditions. Another innovative approach is DROID-SLAM [33], which introduces deep learning to enhance tracking accuracy and the overall robustness of the SLAM system. While these methods have set high benchmarks, they are primarily reliant on feature extraction and matching, which can be challenging in feature-poor or dynamic environments.

NeRF-based SLAM Recent advances in the Neural Radiance Field have shown powerful ability in scene reconstruction. In this evolutionary sequence, NICE-SLAM [45] and iMAP [30] were the first systems to incorporate these concepts, effectively employing NeRF [15] to render intricate environmental geometry by optimizing neural fields. While they established a strong foundation, the lack of robust loop closure detection became apparent. This results in a susceptibility to drift over time, especially in longer sequences or larger environments where re-localization is critical. GO-SLAM [42] introduces loop closure detection based on the previous work. It determines loop closure by detecting co-visibility between the current and historical keyframes and also attempts to map by relying only on RGB inputs. It has made significant progress in solving the scale drift problem, but the lack of the original depth information of the scene in its RGB input mode leads to a large error in scene scale recovery. Subsequently, HI-SLAM [41] emerged, striving to overcome the flaws inherent in GO-SLAM by implementing a more efficient loop closure and a priori depth estimates from Hessian matrices. However, the systems mentioned above are incapable of mapping in unbounded scenes.

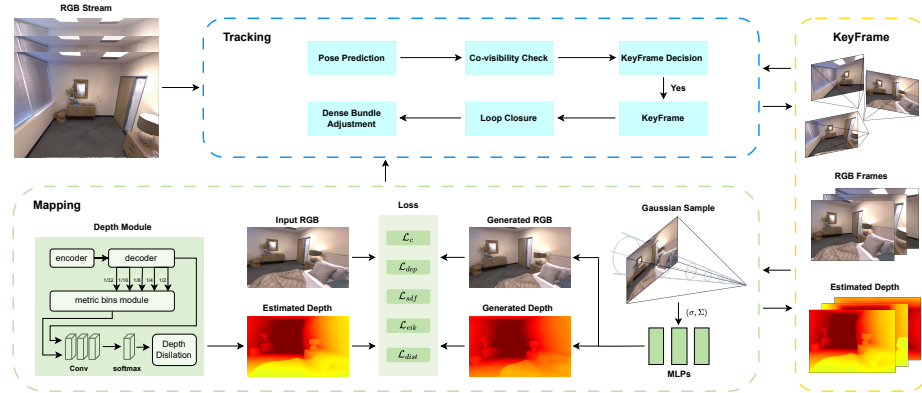


Fig. 2: Overview of MoD-SLAM. We demonstrate the monocular mode of our system, which uses RGB streams as its input. 1) Within the tracking module, the system ascertains the camera poses and depth values while executing loop closure based on a co-visibility check. Simultaneously, it selects keyframes that are subsequently fed into the mapping module. 2) The mapping module leverages the RGB map derived from these keyframes to forecast depth values via a depth estimation module and depth distillation process. Concurrently, Gaussian encoding is applied to the keyframes, and the resultant spatial mean and covariance are fed into MLPs, which in turn enhances the accuracy of scene reconstruction and concurrently refines the pose precision within the tracking module.

3 Method

Fig. 2 shows an overview of our method. For an input RGB stream, we employ a two-step process: first, we estimate the depth values of keyframes using a depth estimator, and subsequently, we refine these depth estimates using depth distillation to filter inaccuracies (Sec. 3.1). We employ a Gaussian spatial information collection approach within the region to capture both the geometric structure and the visual appearance of the scene. In the case of a scene without distinct boundaries, we employ a contraction function to learn long-range spatial information (Sec. 3.2). Specifically, we achieve loop closure detection to eliminate scene drift (Sec. 3.3). Finally, employing a NeRF-based volume rendering method (Sec. 3.4), we generate color and depth values for each pixel, facilitating system network optimization (Sec. 3.5).

3.1 Prior Depth Estimation

Our proposed monocular SLAM system contains a depth estimation module and a depth distillation module. More precisely, the input RGB stream will not only be used as a dataset for NeRF sampling (Sec. 3.2), but will also be fed into

the pre-trained depth estimation module to generate depth information of the scene and put into a depth distillation module to distill depth information subsequently. The use of priori depth estimation significantly enhances the accuracy of scale in scene reconstructed through monocular mode, ensuring that the dimensions of the scene are precisely rendered.

Depth Estimation Fig. 2 shows the components of our depth estimation module. Our depth estimation module contains two parts: relative depth estimation and metric depth estimation. In the relative depth estimation module, we adopt the training criterion of MiDaS [24] and use the DPT decoder-encoder architecture [23] as backbones for feature extraction to predict the relative depths. In the metric depth estimation module, we follow ZoeDepth [3] by proposing the metric bins module to output the metric depth. The metric bins module consists of five heads, which are combined with the relative depths predicted by DPT through convolutional layers and softmax layers to obtain the final depth prediction.

Depth Distillation Due to constraints within the dataset, coarse depth annotations, etc., the depth information derived from single-view depth estimation may deviate from actual depth data. Relying directly on the depth information from the estimation module for supervision could lead to inaccuracies in the reconstructed scene. To address this issue, we introduce a depth distillation module. Building on the foundation laid by prior research [36,18], our module focuses on two key aspects of depth map: spatial continuity and spatial correspondence.

Given a pixel set \mathbf{P} of an RGB image \mathbf{I} , we calculate the depth $\widehat{\mathbf{D}}_k$ of each pixel point $k_n \in \mathbf{P}$. Simultaneously, we extract the depth \mathbf{D}_k which shares the same spatial position as $\widehat{\mathbf{D}}_k$ from the depth estimation module. We ensure the spatial correspondence of the depth map by introducing a spatial correspondence regularization term. We randomly sample two pixels $k_m, k_n \in \mathbf{P}$, the depth spatial correspondence loss is introduced as:

$$\mathcal{L}_{cor} = \frac{1}{M} \sum_{k_m, k_n \in \mathbf{P}} \sum_{\mathbf{D}_{k_m} \leq \mathbf{D}_{k_n}} \max(\widehat{\mathbf{D}}_{k_m} - \widehat{\mathbf{D}}_{k_n} + \tau, 0), \quad (1)$$

where M represents the count of $\mathbf{D}_{k_m} \leq \mathbf{D}_{k_n}$ is observed among the total samples taken. τ is a minimal constant introduced to accommodate slight variations in the depth map. We punish the network if the depth information derived from the depth estimation module lacks spatial correspondence with the depth information obtained through NeRF.

Furthermore, we propose the spatial continuity regularization term to constrain spatial continuity between two depth maps. To achieve it, we randomly sample pixel $k_m \in \mathbf{P}$. Then, within k_m neighboring 3x3 pixel grids, we extract the depth value of each grid denoted as the set Θ_{k_m} . The depth spatial continuity

loss is given by:

$$\mathcal{L}_{con} = \frac{1}{M} \sum_{k_m: T(k_m) \geq 4} \sum_{\mathbf{D}_{k_n} \in \Theta_{k_m}} \max(|\hat{\mathbf{D}}_{k_m} - \hat{\mathbf{D}}_{k_n}| + \tau', 0), \quad (2)$$

where $T(k_m)$ represents the count of $\mathbf{D}_{k_n} \in \Theta_{k_m}$, holding $|\mathbf{D}_{k_m} - \mathbf{D}_{k_n}| < \tau'$ true. τ' signifies a minor margin between the current pixel point and its adjacent pixel points. M denotes the aggregate count of samples satisfying the criteria within set \mathbf{P} . Our method punishes non-continuous depth values at the surface of the geometric object and avoids bias at the edges of the geometric object.

Training Strategy As mentioned above, to enable our depth estimation module to accurately predict depth, we need to pre-train the MiDaS backbones network to predict relative depth as well as the head of the metric bins module to fine-tune the metric depth.

The findings from [3,13] indicate that utilizing a singular metric head across various datasets fails to yield effective predictions. Therefore, our model uses multiple metric heads. These different metric heads are used for metric depth prediction in different datasets, which requires us to train different metric heads using different datasets. In addition, because our model incorporates relative depth pretraining, it can also solve the problem of fine-tuning the relative depth backbone in different scenes to some extent.

3.2 Scene Representation

Multivariate Gaussian Encoding NeRF constructs the training dataset by projecting a fine ray to the center of each pixel point and then performing coarse and fine sampling. This sampling strategy enriches the approach to some extent by integrating all the sampled points on the ray to obtain the color of a pixel. However, it also leads to missing information. This is because the number of sampled points is limited, and the ray fails to encapsulate information within the three-dimensional space surrounding the sampled points. Inspired by the Mip-NeRF [1], we direct a cone-shaped projection to the pixel rather than slender rays. Projecting the cone allows us to collect more detailed information in the three-dimensional space and transfer it to MLPs for training. The training speed of the model is also greatly improved by eliminating the coarse and fine sampling processes.

To compute the above features, we approximate the conic truncation with a multivariate Gaussian to compute the features in a particular space. To enhance the system's stability, particularly in scenarios demanding higher accuracy and more sampling points, we address a critical issue. The proximity of neighboring sampling points, denoted as t_0 and t_1 , often results in a minimal distance $t_1 - t_0$, which can compromise stability during division. Consequently, we introduce $t_\mu = (t_0 + t_1)/2$ and $t_\delta = (t_0 - t_1)/2$ as refined parameters to bolster the system's stability. We assume that cone truncations are all symmetric for the cone center axis, then the multivariate Gaussian features are represented by three variables:

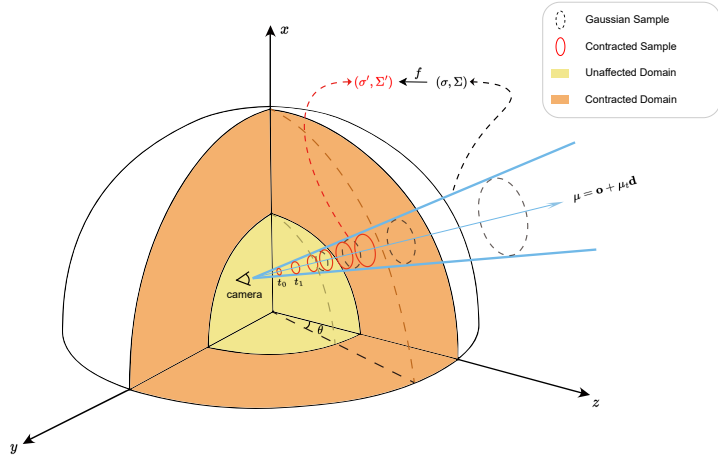


Fig. 3: Scene Reparameterization. To manage unbounded scenes, we use a contract function to map mean and covariance data from spatial sampling (black dashed line) directly to a new range (red solid line). We ignore the data within the sphere of radius 1 (yellow region) while mapping the data from regions beyond a radius of 1 into the spherical coordinate system with a radius of 2 (orange region).

the mean distance along the ray μ_t , the variance along the ray σ_t^2 , and the variance perpendicular to the ray σ_r^2 :

$$\mu_t = t_\mu + \frac{2t_\mu t_\delta^2}{3t_\mu^2 + t_\delta^2}, \quad \sigma_t^2 = \frac{t_\delta^2}{3} - \frac{4t_\delta^4(12t_\mu^2 - t_\delta^2)}{15(3t_\mu^2 + t_\delta^2)^2}, \quad (3)$$

$$\sigma_r^2 = r^2 \left(\frac{t_\delta^2}{4} + \frac{5t_\delta^2}{12} - \frac{4t_\delta^4}{15(3t_\mu^2 + t_\delta^2)} \right), \quad (4)$$

r is the perpendicular distance between the sampling plane where the ray is located and the ray at the center of the pixel point after transformation by spherical coordinates. Define the position of the origin of the camera in the world coordinate system as $\mu = \mathbf{o} + \mu_t \mathbf{d}$. All of the above are functional relationships obtained in the camera coordinate system. To determine the position of the pixel point in the world coordinate system more rationally, we transform the mean and covariance of the variables expressing the multivariate Gaussian from the camera coordinate system to the world coordinate system as follows:

$$\sigma = \mathbf{d}\mu_t, \quad \Sigma = \mu_r(\mathbf{I} - \mathbf{d}\mathbf{d}^T) + \mu_t \mathbf{d}\mathbf{d}^T, \quad (5)$$

following the above equations, we can obtain a multivariate Gaussian representation for the position as well as the direction in a particular space.

Unbounded Scenes Previous research [2] has demonstrated that the predictive efficacy of MLPs significantly diminishes when applied to datasets characterized by large disparities. Thus, for bounded scenes, a normalization method is generally used to restrict all the data in the training set to a specific region to enhance the predictive capability of MLPs. Nevertheless, for scenes without defined boundaries, normalization of the scene is impracticable owing to the lack of essential boundary scale information. Therefore, we define $f(\mathbf{x})$ to reparameterize the data as follows:

$$f(\mathbf{x}) = \lambda \mathbf{x} + (1 - \lambda) \left(2 - \frac{1}{\|\mathbf{x}\|} \right) \left(\frac{\mathbf{x}}{\|\mathbf{x}\|} \right), \quad \lambda = \begin{cases} 1 & \|\mathbf{x}\| \leq 1 \\ 0 & \|\mathbf{x}\| > 1 \end{cases} \quad (6)$$

This can be interpreted as an extension of the normalized device coordinate (NDC). We make the scene shrink along the inverse depth direction, thus enabling the network to train on and interpret unbounded geometric scenes. However, since in Equ. 5 above we used the mean and covariance to represent information about the cross-section within the conic, we also need to map the mean and covariance to it.

To achieve this, first, we linearize $f(\mathbf{x})$ by performing a first-order Taylor expansion at the point μ :

$$f(\mathbf{x}) = f(\mu) + \mathbf{J}_f(\mu)(\mathbf{x} - \mu), \quad (7)$$

where $\mathbf{J}_f(\mu)$ is the jacobian of f at μ . After doing that, we can obtain mean function $E(\mathbf{x})$ and covariance function $D(\mathbf{x})$ as:

$$f(E(\mathbf{x}), D(\mathbf{x})) = \begin{cases} E(\mathbf{x}) : f(\mu) \\ D(\mathbf{x}) : \mathbf{J}_f(\mu)D(\mathbf{x})\mathbf{J}_f(\mu)^T, \end{cases} \quad (8)$$

our choice for f is relied on Equ. 6.

3.3 Loop Closure

SLAM calculates the camera's position for the next frame based on the position of the previous frame, resulting in the accumulation of errors. Loop closure detection is introduced to eliminate the drift. Our system is divided into four stages: loop closure candidate frame detection, *sim3* change calculation, loop closure fusion and pose optimization. For the current key frame K_i , we find the best three loop closure candidates and fusion candidates K_m based on the similarity. Then for each candidate frame, we define a localized window containing 5 keyframes with the highest covariance with the candidate frame and the map points. To avoid false positives, the loop closure candidate frames are further subjected to covariance geometry checking as well as timing geometry checking. After that, the loop closure candidate frames selected after verification are used to construct a local window with the current keyframes for map fusion. Finally, the keyframes are optimized to eliminate the drift during tracking.

3.4 Depth and Color Rendering

Inspired by the recent work in NeRF, we propose to also use Neural radiance field to reconstruct 3D scenes.

Given the current camera pose and camera intrinsic matrix, we can calculate the viewing direction \mathbf{r} and change it to world coordinate. Unlike NeRF, since our system is also used to process borderless scenes at the same time, we propose here a more efficient sampling technique, the differential sampling technique. This sampling technique aims to sample more in the near part of the ray and sparsely in the far part. To accomplish this idea, we first sample the ray at the proximal n as well as at the distal f , and then obtain a series of sampling points by sampling uniformly in this space $\{s_1, \dots, s_N\}$. After that, we map the sampling points to the following function:

$$s' = \frac{1}{s^{\frac{1}{f}} + (1 - s)^{\frac{1}{n}}}, \quad (9)$$

and then we get the new sampling points as $\{s'_1, \dots, s'_N\}$.

To complete the scene reconstruction, we randomly extract N rays and M pixel points in the current frame and keyframes. We input the position set \mathbf{P} to the depth prediction unit in Sec. 3.1 to get the true depth \mathbf{D} . We do a multivariate Gaussian variation of the pose set \mathbf{G} in Sec. 3.2 to get the mean as well as the covariance set. The mean and covariance are then passing into the MLPs to obtain the predicted volume density as well as the predicted color. Volume density is used to calculate the occupancy probability o_i and the ray termination probability at each sample can then be calculated as $w_i = o_i \prod_{i=j}^{i-1} (1 - o_j)$. Eventually, the depth and color can be rendered as:

$$\widehat{\mathbf{D}} = \sum_{k=1}^N w_i d_i, \quad \widehat{\mathbf{C}} = \sum_{k=1}^N w_i c_i, \quad (10)$$

where d_i is the corresponding depth values of sampling points and c_i is the rgb values of sampling points.

3.5 Tracking and Mapping

Camera Tracking For more accurate position tracking, in this work, we employ DROID-SLAM [33] as the front end of our system due to its superior position prediction capabilities and minimal position drift. We take the video stream as input, and for each frame maintain two state variables: camera position and inverse depth. The pose set $\{\mathbf{G}_t\}_{t=0}^N$ and the inverse depth set $\{\mathbf{d}_t\}_{t=0}^N$ are unknown state variables, which are iteratively updated during the inference process of processing a new frame. Each input image is processed through a feature extraction network with a context network. The feature extraction network consists of 6 residual blocks and 3 downsampling layers to generate a dense feature map for each image.

In the network training phase, we train our network by using a combination of pose loss and depth loss. We pre-compute a distance matrix of size $\mathbf{K} * \mathbf{K}$, where \mathbf{K} is the length of each input image. This matrix is used to store the size of the average optical flow between each pair of frames. Then, we compute the depth loss \mathcal{L}_d generated by the predicted depth and the true depth, and the position pose loss \mathcal{L}_v generated by the predicted bit pose and the true position pose. The loss is taken as the average l2 distance between the two optical flow fields [40]:

$$\mathcal{L}_{tracking} = \mathcal{L}_v + \lambda_v \mathcal{L}_d, \quad (11)$$

where λ_v is a weight used to limit the depth loss to the overall tracking loss. In this system, we take λ_v equals to 0.1.

Mapping To enhance the fidelity of the reconstructed scene to the actual scene, we initially sample M pixels from the keyframes. Subsequently, the network can be optimized by minimizing the loss.

We use the method mentioned in [16] to render the color of the pixel point $\widehat{\mathbf{C}}$. To optimize the network, we minimize the loss between the predicted color and the true color:

$$\mathcal{L}_{rgb} = \frac{1}{M} \sum_{m=1}^M |\widehat{\mathbf{C}}_m - \mathbf{C}_m|, \quad (12)$$

We also use Equ. 1 and Equ. 2 to constrain depth value to supervise the reconstruction of this system and better recover the scale:

$$\mathcal{L}_{depth} = \mathcal{L}_{cor} + \lambda_{con} \mathcal{L}_{con}, \quad (13)$$

where λ_{con} denotes the hyperparameter employed to modulate the weight of \mathcal{L}_{depth} . Furthermore, following [2], we also introduce distortion loss, which is used to eliminate artifacts in pictures caused by discontinuities in volume density over tiny areas. Distortion loss is defined as:

$$\mathcal{L}_{dist} = \sum_{i,j} w_i w_j \left| \frac{s_i + s_{i+1}}{2} - \frac{s_j + s_{j+1}}{2} \right| + \sum_i \frac{1}{3} w_i^2 (s_{i+1} - s_i), \quad (14)$$

where the first term minimizes the weighted distance between pairs of points in all intervals and the second term minimizes the weighted size of each individual interval. Additionally, following [10], regularization to the predicted SDF is also introduced in this system. At each iteration, we can get the predicted signed distance of given batch points as: $\widehat{\xi} = f(s; \theta)$. To encourage valid SDF values, especially in unsupervised areas, we adopt the Eikonal term:

$$\mathcal{L}_{eik} = \frac{1}{MN_{ray}} \sum_{m=1}^M \sum_{i \in N} (1 - \|\nabla \phi(\mathbf{s}_i)\|)^2. \quad (15)$$

For the SDF, we approximate the SDF values by calculating the depth values along the observation direction as: $\mathbf{b}(\mathbf{s}) = \widehat{\mathbf{D}} - \mathbf{D}$. We then define the adopted loss

function by its distance from the surface. For $|\phi(\mathbf{s})| \leq |\mathbf{b}(\mathbf{s})|, \forall \mathbf{s}$, the near-surface points($\widehat{\mathbf{D}} - \mathbf{D} \leq \zeta$), following [21,38] the SDF loss is:

$$\mathcal{L}_{sdf} = \frac{1}{MN_{ray}} \sum_{m=1}^M \sum_{i \in N} |\phi(\mathbf{s}_i) - \mathbf{b}(\mathbf{s}_i)|, \quad (16)$$

for the other situation, the far-surface points($\widehat{\mathbf{D}} - \mathbf{D} > \zeta$), the SDF loss is:

$$\mathcal{L}_{sdf} = \frac{1}{MN_{ray}} \sum_{m=1}^M \sum_{i \in N} \max(0, e^{-\alpha\phi(\mathbf{s}_i)}, \phi(\mathbf{s}_i) - \mathbf{b}(\mathbf{s}_i)), \quad (17)$$

where we set α equal to 5 in this system. In our approach, the treatment of SDF predictions varies based on their values: no penalty is imposed when the prediction is positive and falls below a specified bound; a linear loss is introduced for larger SDF predictions; and, in cases where the prediction is negative, an exponential penalty is applied to ensure smooth transitions between these states.

Our real-time mapping thread optimizes the predicted neural networks by continuously feeding keyframes to achieve ideal 3D reconstruction results. The total loss of the system is:

$$\mathcal{L}_{total} = \lambda_c \mathcal{L}_c + \lambda_{dep} \mathcal{L}_{dep} + \lambda_{dist} \mathcal{L}_{dist} + \lambda_{eik} \mathcal{L}_{eik} + \lambda_{sdf} \mathcal{L}_{sdf}, \quad (18)$$

where $\lambda_c, \lambda_{depth}, \lambda_{dist}, \lambda_{eik}, \lambda_{sdf}$ are the hyperparameters for each loss, controlling the weight of each loss in the total loss.

4 Experiments

We evaluate our models in both synthetic and real-world datasets, including Replica [28] and ScanNet [7]. We also conducted a comparative analysis of the reconstruction quality of our system against state-of-the-art SLAM systems and executed ablation studies to validate the soundness of our model’s architecture.

4.1 Experimental Setup

Datasets For our quantitative analysis, we implement our system on the Replica dataset and ScanNet dataset. We follow the same pre-processing step for datasets as in NICE-SLAM [45]. Each dataset presents challenging camera dynamics, effectively showcasing our model’s performance. We concurrently utilize these datasets to assess our model in both monocular RGB and RGB-D modes.

Metrics In evaluating camera tracking accuracy, we follow standard SLAM metrics. This involves comparing the trajectory of keyframes against the true trajectory and computing the Root Mean Square Error (RMSE) of the Absolute Trajectory Error (ATE) [29]. Regarding reconstruction quality, we evaluate it by accuracy [cm], PSNR [9], SSIM and F-score [$< 5\text{cm } \%$] [30]. In addition, we

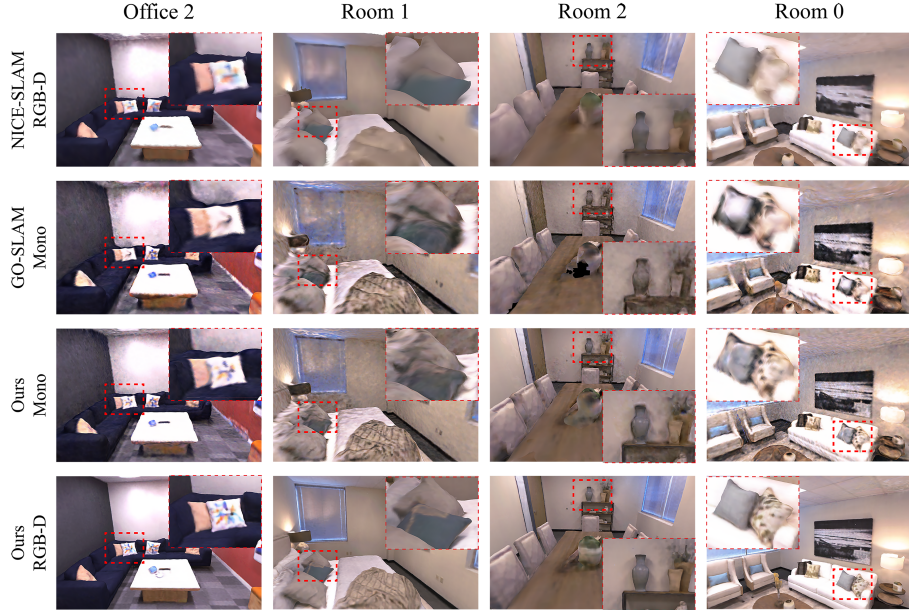


Fig. 4: Reconstruction results on Replica [28]. Compared with baselines, the 3D scenes reconstructed by our method achieve better geometric structure and texture features.

evaluate the L1 loss [45] between the reconstructed and real meshes. All our experimental results are averaged after three runs.

Implementation Details We run our system on a PC with a 4.70 GHz AMD 7900X CPU and NVIDIA RTX 4090 GPU. We use the pre-trained model from DROID-SLAM [33] for tracking and use the same parameters in the tracking process as it. In the reconstruction process, we choose to sample a ray at several points of $N_{strat} = 20$ and $N_{imp} = 40$. For Replica, we sample $M = 300$ pixels, while for Scan-Net, we sample $M = 600$ pixels. For loss weights, we choose $\lambda_c = 1.0$, $\lambda_{dep} = 1.0$, $\lambda_{dist} = 0.002$, $\lambda_{eik} = 0.15$, $\lambda_{sdf} = 1.0$. The compared baseline includes classical SLAM systems ORB-SLAM3 [4] and DROID-SLAM [30], newest SLAM systems NICE-SLAM [45], HI-SLAM [41] and GO-SLAM [42] and 3D Gaussian-based SLAM Photo-SLAM [11].

4.2 Results and Evaluation

Evaluation on Replica [28] Replica includes several geometric models reconstructed from real-world scenes. Table 2 shows the results of the reconstruction of systems on the Replica dataset. Compared to the systems mentioned in the



Fig. 5: Reconstruction results on ScanNet [7]. Compared with baselines, our system demonstrates enhanced capability in scale recovery and void interpolation within the scene.

table, our system exhibits superior tracking capabilities in both monocular and RGB-D modes. In comparison with NeRF-based SLAM systems [45, 42, 44], our approach achieves enhanced reconstruction fidelity. Compared to 3D Gaussian-based SLAM systems [11], our system falls in terms of scene reconstruction accuracy. However, our system outperforms in tracking performance and is more effective in recovering the scale of the scene. Fig. 4 and Fig. 6(a) present a comparative analysis of scene reconstructions by our system against NICE-SLAM [45] and GO-SLAM [42]. Our method demonstrates superior performance that shows smoother scene reconstruction and the ability to restore the texture and contours of geometric objects more accurately.

Evaluation on ScanNet [7] We evaluated our system across seven distinct scenes in ScanNet dataset [7]. Table 2 presents the tracking results. Our system outperforms others in tracking accuracy, particularly in the large indoor scenes of ScanNet. As illustrated in Fig. 5, our system outmatches GO-SLAM [42] by rendering the scene with enhanced detail fidelity, more accurately approximating the real-world geometry and ensuring smoother scene transitions. Furthermore, our framework possesses a pronounced proficiency in addressing scene sparsity through effective void interpolation.

4.3 Ablation Study

In this section, we evaluate the choice of our depth estimation module, multivariate Gaussian encoding and reparameterization.

Mode	Method	ATE[cm]↓	L1[cm]↓	ACC.↓	PSNR↑	SSIM↑	FPS↑
RGB-D	NICE-SLAM[45]	1.95	3.53	2.85	26.31	0.847	0.3
	Go-SLAM[42]	0.34	3.38	2.50	27.38	0.851	8
	Ours	0.33	3.21	2.29	29.95	0.862	6
Mono	DROID-SLAM[33]	0.42	-	5.03	-	-	21
	NICER-SLAM[44]	1.88	x	3.65	25.41	0.827	6
	GO-SLAM[42]	0.39	4.39	3.81	22.13	0.733	8
	Photo-SLAM[11]	1.09	x	x	33.30	0.930	42
	Ours	0.35	3.40	2.68	27.31	0.850	8

Table 1: Reconstruction quality and run-time comparison on Replica [28]. Our results were obtained by averaging three runs across seven scenes from the Replica dataset. '-' indicates the inability to acquire pertinent data. 'x' denotes data that has yet to be released.

	Scene ID	0000	0059	0106	0169	0181	0207	0233	Avg.
Mono	DROID-SLAM[45]	5.48	9.00	7.86	7.41	5.43	72.23	6.76	16.31
	Go-SLAM[42]	5.94	8.27	8.42	8.29	7.48	5.31	8.07	7.40
	Ours	5.39	7.78	7.44	6.69	3.97	5.63	6.58	6.22
RGBD	NICE-SLAM[45]	8.64	12.25	10.28	12.93	5.59	10.53	8.09	9.76
	GO-SLAM[42]	5.35	7.52	7.74	6.84	3.47	4.78	7.03	6.10
	Co-SLAM[37]	7.13	11.14	5.90	11.81	7.14	8.75	9.36	8.75
	E-SLAM[12]	7.32	8.57	6.53	9.0	5.74	7.96	7.51	7.52
	Ours	5.27	7.44	6.73	6.48	3.29	5.31	6.14	5.81

Table 2: ATE RMSE [cm] on the ScanNet dataset [7]. The performance metrics reported by our system for each scene are derived from the average of three executions per scene.

Depth Estimation We investigate the effect of the depth prediction module and depth distillation on the performance of our system. Table 4 shows the reconstruction performance of the system in monocular mode with the depth estimation module removed and the depth estimation module incorporated. Without the depth estimation module, our system suffers a dramatic drop in both tracking and mapping performance. However, with the cooperation of the depth estimation module and depth distillation module, the monocular mode performance of our system closely approaches that of the RGB-D mode.

Losses We further evaluate the impact of each loss on the reconstruction performance of the system. Table 3 shows the impact of each loss on the reconstruction performance of the system, and it's easy to find that only by relying on \mathcal{L}_c and \mathcal{L}_{depth} cannot lead to the best reconstruction result. \mathcal{L}_{sdf} has a more significant impact on the improvement of reconstruction quality because it affects the

\mathcal{L}_c	\mathcal{L}_{dep}	\mathcal{L}_{eik}	\mathcal{L}_{sdf}	\mathcal{L}_{dist}	Avg. F-score↑	PSNR↑
1	0	0	0	0	31.33	15.08
1	1	0	0	0	85.19	26.76
1	1	1	0	0	85.42	26.88
1	1	1	1	0	88.03	27.59
1	1	1	1	1	88.73	27.84

Table 3: The impact of various losses. All data are averaged over three runs in monocular mode on our system under seven scenes of the Replica dataset. '1' represents use this loss while '0' means ignore.

	ATE[cm]↓	F-score↑
None	0.46	82.93
DepE.	0.39	86.66
DepE./DepD.	0.35	88.73
RGB-D	0.33	89.96

Table 4: Depth ablation study. We explore the effects of the depth estimation module (DepE.) and the depth distillation module (DepD.) in our system.

	PSNR↑	SSIM↑
Con.	23.25	0.722
Con-Gau.	24.14	0.757
None	-	-
NEWTON[14]	23.15	0.702

Table 5: Unbounded scene ablation study. We investigate the effects of the constructed function (Con.) and Gaussian encoding (Gau.) in our system.

expression and reconstruction of the object’s geometric surface information. In addition, \mathcal{L}_{eik} and \mathcal{L}_{dist} also have a positive impact on improving the reconstruction performance, one of them is used to optimize the geometric surface and the other is used to eliminate artifacts. Integrating all terms produces the best result.

Unbounded Scene We also conduct tests to assess the impact of reparameterization Equ. 6 and Gaussian encoding Equ. 5 on reconstructing scenes with no defined boundaries. For comparison, we used NEWTON [14] as a baseline to evaluate our system’s performance. The quantitative data in Table 5 indicates that our reparameterization and Gaussian encoding significantly improve the accuracy in both scaling and geometric reconstruction of unbounded scenes. These approaches notably enhance our system’s overall performance. Our data were acquired using the RGB-D mode of our system within the ScanNet 0207 scene. NEWTON’s data are from the original paper [14]. The results on the ScanNet [7] indicate that our model shows greater robustness and more precise tracking abilities compared to NEWTON.

4.4 Runtime Analysis

We test the tracking and the mapping time of NICER-SLAM [44], GO-SLAM [42] and our system using the same number of sampling points. Fig. 6(b) shows that our system is faster than GO-SLAM and NICER-SLAM in tracking process.

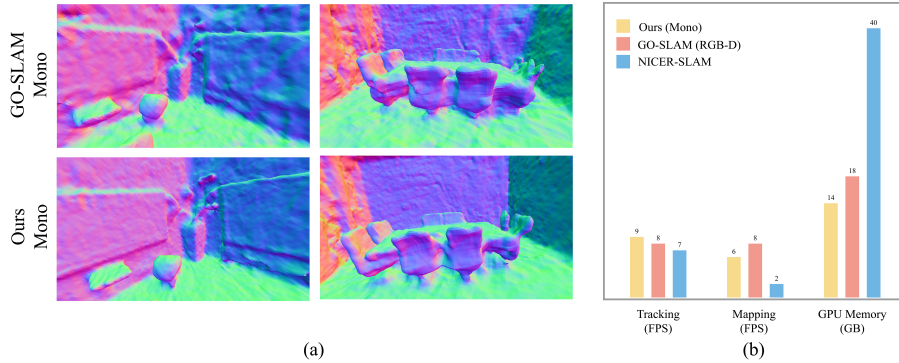


Fig. 6: (a) shows the reconstruction result on Replica. (b) shows the run time and GPU memory used in SLAM systems.

However, because of the depth estimation module, our system is slightly slower than GO-SLAM in mapping process, but the higher than NICER-SLAM. In addition, Fig. 6 also demonstrates that our model size is maller and uses less memory. GO-SLAM and our system are benchmarked with an NVIDIA RTX 4090 GPU while NICER-SLAM is benchmarked with an A100.

5 Conclusion

We presented MoD-SLAM, a monocular implicit neural-based dense mapping method that improves both the speed and accuracy of NeRF-based SLAM systems. Our experiments demonstrate that by integrating a monocular depth estimation module, our system not only achieves a more accurate scene-scale reconstruction but also excels in reconstructing the details and textures of geometric objects compared to previous SLAM systems. Additionally, we show the superior performance of our system in reconstructing unbounded scenes after employing Gaussian encoding and reparametrization techniques.

Limitations The depth estimation module relies on a pre-trained model; thus, for complex scenes or those significantly divergent from our provided pre-trained scenes, it's necessary to retrain the depth estimation module. Moreover, compared to traditional SLAM, our method lacks an IMU [32] module, leading to tracking errors. Finally, the integration of depth estimation in mapping under monocular mode results in a slower mapping speed.

References

1. Barron, J.T., Mildenhall, B., Tancik, M., Hedman, P., Martin-Brualla, R., Srinivasan, P.P.: Mip-nerf: A multiscale representation for anti-aliasing neural radiance fields. 2021 IEEE/CVF International Conference on Computer Vision (ICCV) (2021) [1](#), [6](#)
2. Barron, J.T., Mildenhall, B., Verbin, D., Srinivasan, P.P., Hedman, P.: Mip-nerf 360: Unbounded anti-aliased neural radiance fields. 2022 IEEE/CVF Conference on Computer Vision and Pattern Recognition (CVPR) (2021) [8](#), [10](#)
3. Bhat, S., Birk, R., Wofk, D., Wonka, P., Muller, M.: Zoedepth: Zero-shot transfer by combining relative and metric depth. ArXiv (2023) [5](#), [6](#)
4. Campos, C., Elvira, R., Rodríguez, J.J.G., Montiel, J.M.M., Tardós, J.D.: Orb-slam3: An accurate open-source library for visual, visual-inertial, and multimap slam. IEEE Transactions on Robotics **37**, 1874–1890 (2020) [1](#), [3](#), [12](#)
5. Chen, J., Bautembach, D., Izadi, S.: Scalable real-time volumetric surface reconstruction. ACM Trans. Graph. (2013) [3](#)
6. Chung, C.M., Tseng, Y.C., Hsu, Y.C., Shi, X.Q., Hua, Y.H., Yeh, J.F., Chen, W.C., Chen, Y.T., Hsu, W.H.: Orbeez-slam: A real-time monocular visual slam with orb features and nerf-realized mapping. 2023 IEEE International Conference on Robotics and Automation (ICRA) (2022) [2](#)
7. Dai, A., Chang, A.X., Savva, M., Halber, M., Funkhouser, T.A., Nießner, M.: Scan-net: Richly-annotated 3d reconstructions of indoor scenes. 2017 IEEE Conference on Computer Vision and Pattern Recognition (CVPR) (2017) [11](#), [13](#), [14](#), [15](#)
8. Deng, K., Liu, A., Zhu, J.Y., Ramanan, D.: Depth-supervised nerf: Fewer views and faster training for free. 2022 IEEE/CVF Conference on Computer Vision and Pattern Recognition (CVPR) (2021) [1](#)
9. Fardo, F.A., Conforto, V.H., de Oliveira, F.C., Rodrigues, P.S.S.: A formal evaluation of psnr as quality measurement parameter for image segmentation algorithms. ArXiv (2016) [11](#)
10. Gropp, A., Yariv, L., Haim, N., Atzmon, M., Lipman, Y.: Implicit geometric regularization for learning shapes. ArXiv (2020) [10](#)
11. Huang, H., Li, L., Cheng, H., Yeung, S.K.: Photo-slam: Real-time simultaneous localization and photorealistic mapping for monocular, stereo, and rgbd cameras. ArXiv (2023) [12](#), [13](#), [14](#)
12. Johari, M.M., Carta, C., Fleuret, F.: Eslam: Efficient dense slam system based on hybrid representation of signed distance fields. 2023 IEEE/CVF Conference on Computer Vision and Pattern Recognition (CVPR) (2022) [14](#)
13. Li, Z., Bhat, S.F., Wonka, P.: Patchfusion: An end-to-end tile-based framework for high-resolution monocular metric depth estimation. ArXiv (2023) [6](#)
14. Matsuki, H., Tateno, K., Niemeyer, M., Tombari, F.: Newton: Neural view-centric mapping for on-the-fly large-scale slam. ArXiv (2023) [15](#)
15. Mildenhall, B., Srinivasan, P.P., Tancik, M., Barron, J.T., Ramamoorthi, R., Ng, R.: Nerf: Representing scenes as neural radiance fields for view synthesis. Commun. ACM (2020) [1](#), [3](#)
16. Müller, T., Evans, A., Schied, C., Keller, A.: Instant neural graphics primitives with a multiresolution hash encoding. ACM Transactions on Graphics (TOG) (2022) [10](#)
17. Mur-Artal, R., Tardós, J.D.: Orb-slam2: An open-source slam system for monocular, stereo, and rgbd cameras. IEEE Transactions on Robotics (2016) [1](#)
18. Niemeyer, M., Barron, J.T., Mildenhall, B., Sajjadi, M.S.M., Geiger, A., Radwan, N.: Regnerf: Regularizing neural radiance fields for view synthesis from sparse

inputs. 2022 IEEE/CVF Conference on Computer Vision and Pattern Recognition (CVPR) (2021) 5

19. Niemeyer, M., Mescheder, L.M., Oechsle, M., Geiger, A.: Differentiable volumetric rendering: Learning implicit 3d representations without 3d supervision. 2020 IEEE/CVF Conference on Computer Vision and Pattern Recognition (CVPR) (2019) 1

20. Nießner, M., Zollhöfer, M., Izadi, S., Stamminger, M.: Real-time 3d reconstruction at scale using voxel hashing. ACM Trans. Graph. (2013) 3

21. Ortiz, J., Clegg, A., Dong, J., Sucar, E., Novotný, D., Zollhoefer, M., Mukadam, M.: isdf: Real-time neural signed distance fields for robot perception. ArXiv (2022) 11

22. Park, J.J., Florence, P.R., Straub, J., Newcombe, R.A., Lovegrove, S.: Deepsdf: Learning continuous signed distance functions for shape representation. 2019 IEEE/CVF Conference on Computer Vision and Pattern Recognition (CVPR) (2019) 2

23. Ranftl, R., Bochkovskiy, A., Koltun, V.: Vision transformers for dense prediction. 2021 IEEE/CVF International Conference on Computer Vision (ICCV) (2021) 5

24. Ranftl, R., Lasinger, K., Hafner, D., Schindler, K., Koltun, V.: Towards robust monocular depth estimation: Mixing datasets for zero-shot cross-dataset transfer. IEEE Transactions on Pattern Analysis and Machine Intelligence (2019) 5

25. Rosinol, A., Leonard, J.J., Carbone, L.: Nerf-slam: Real-time dense monocular slam with neural radiance fields. 2023 IEEE/RSJ International Conference on Intelligent Robots and Systems (IROS) (2022) 2

26. Sitzmann, V., Martel, J.N.P., Bergman, A.W., Lindell, D.B., Wetzstein, G.: Implicit neural representations with periodic activation functions. ArXiv (2020) 1

27. Stotko, P., Krumpen, S., Hullin, M.B., Weinmann, M., Klein, R.: Slamcast: Large-scale, real-time 3d reconstruction and streaming for immersive multi-client live telepresence. IEEE Transactions on Visualization and Computer Graphics (2018) 3

28. Straub, J., Whelan, T., Ma, L., Chen, Y., Wijmans, E., Green, S., Engel, J.J., Mur-Artal, R., Ren, C.Y., Verma, S., Clarkson, A., Yan, M., Budge, B., Yan, Y., Pan, X., Yon, J., Zou, Y., Leon, K., Carter, N., Briales, J., Gillingham, T., Mueggler, E., Pesqueira, L., Savva, M., Batra, D., Strasdat, H.M., Nardi, R.D., Goesele, M., Lovegrove, S., Newcombe, R.A.: The replica dataset: A digital replica of indoor spaces. ArXiv (2019) 11, 12, 14

29. Sturm, J., Engelhard, N., Endres, F., Burgard, W., Cremers, D.: A benchmark for the evaluation of rgbd slam systems. 2012 IEEE/RSJ International Conference on Intelligent Robots and Systems (2012) 11

30. Sucar, E., Liu, S., Ortiz, J., Davison, A.J.: imap: Implicit mapping and positioning in real-time. 2021 IEEE/CVF International Conference on Computer Vision (ICCV) (2021) 2, 3, 11, 12

31. Sucar, E., Wada, K., Davison, A.J.: Nodeslam: Neural object descriptors for multi-view shape reconstruction. 2020 International Conference on 3D Vision (3DV) (2020) 1

32. Tedaldi, D., Pretto, A., Menegatti, E.: A robust and easy to implement method for imu calibration without external equipments. In: 2014 IEEE International Conference on Robotics and Automation (ICRA) (2014) 16

33. Teed, Z., Deng, J.: Droid-slam: Deep visual slam for monocular, stereo, and rgbd cameras. In: Neural Information Processing Systems (2021) 3, 9, 12, 14

34. Tolstikhin, I.O., Houlsby, N., Kolesnikov, A., Beyer, L., Zhai, X., Unterthiner, T., Yung, J., Keysers, D., Uszkoreit, J., Lucic, M., Dosovitskiy, A.: Mlp-mixer: An all-mlp architecture for vision. In: Neural Information Processing Systems (2021) [2](#)
35. Vespa, E., Nikolov, N., Grimm, M., Nardi, L., Kelly, P.H.J., Leutenegger, S.: Efficient octree-based volumetric slam supporting signed-distance and occupancy mapping. IEEE Robotics and Automation Letters (2018) [3](#)
36. Wang, G., Chen, Z., Loy, C.C., Liu, Z.: Sparsenerf: Distilling depth ranking for few-shot novel view synthesis. 2023 IEEE/CVF International Conference on Computer Vision (ICCV) (2023) [5](#)
37. Wang, H., Wang, J., de Agapito, L.: Co-slam: Joint coordinate and sparse parametric encodings for neural real-time slam. 2023 IEEE/CVF Conference on Computer Vision and Pattern Recognition (CVPR) (2023) [2, 14](#)
38. Wang, J., Bleja, T., de Agapito, L.: Go-surf: Neural feature grid optimization for fast, high-fidelity rgb-d surface reconstruction. 2022 International Conference on 3D Vision (3DV) (2022) [11](#)
39. Zeng, M., Zhao, F., Zheng, J., Liu, X.: Octree-based fusion for realtime 3d reconstruction. Graph. Models (2013) [3](#)
40. Zhang, T., Zhang, H., Li, Y., Nakamura, Y., Zhang, L.: Flowfusion: Dynamic dense rgb-d slam based on optical flow. 2020 IEEE International Conference on Robotics and Automation (ICRA) (2020) [10](#)
41. Zhang, W., Sun, T., Wang, S., Cheng, Q., Haala, N.: Hi-slam: Monocular real-time dense mapping with hybrid implicit fields. IEEE Robotics and Automation Letters (2023) [2, 3, 12](#)
42. Zhang, Y., Tosi, F., Mattoccia, S., Poggi, M.: Go-slam: Global optimization for consistent 3d instant reconstruction. 2023 IEEE/CVF International Conference on Computer Vision (ICCV) (2023) [2, 3, 12, 13, 14, 15](#)
43. Zhi, S., Bloesch, M., Leutenegger, S., Davison, A.J.: Scenecode: Monocular dense semantic reconstruction using learned encoded scene representations. 2019 IEEE/CVF Conference on Computer Vision and Pattern Recognition (CVPR) (2019) [1](#)
44. Zhu, Z., Peng, S., Larsson, V., Cui, Z., Oswald, M.R., Geiger, A., Pollefeys, M.: Nicer-slam: Neural implicit scene encoding for rgb slam. ArXiv (2023) [13, 14, 15](#)
45. Zhu, Z., Peng, S., Larsson, V., Xu, W., Bao, H., Cui, Z., Oswald, M.R., Pollefeys, M.: Nice-slam: Neural implicit scalable encoding for slam. 2022 IEEE/CVF Conference on Computer Vision and Pattern Recognition (CVPR) (2021) [2, 3, 11, 12, 13, 14](#)
46. Zubizarreta, J.A., Aguinaga, I., Montiel, J.M.M.: Direct sparse mapping. IEEE Transactions on Robotics **36**, 1363–1370 (2019) [1](#)